Journal of The Electrochemical Society, **165** (10) C689-C702 (2018)

Solute Capture and Doping of Al in Cu_2O: Corrosion, Tarnish Resistance, and Cation Release of High-Purity Cu-Al Alloys in Artificial Perspiration

M. J. Hutchison [*,z] **and J. R. Scully** [**]

Department of Materials Science and Engineering, University of Virginia, Charlottesville, Virginia 22904, USA

Frequently-touched surfaces are a common transmission source for hospital and community acquired infections. Cu alloys have shown promise as antimicrobial surfaces, able to kill even antibiotic-resistant bacteria within minutes. However, the most efficacious alloy systems readily tarnish making them unsuitable for hospital applications and tarnish-resistant (e.g., passive) systems often cannot maintain sufficient Cu ion release to maintain antimicrobial function. An ideal alloy would have optimal corrosion, tarnishing, and Cu release tuned through alloying elements. Cu-Al alloys are tarnish-resistant, yet the precise role of Al remains unclear. High-purity binary alloys of Cu-Al were fully immersed in artificial perspiration at open circuit to evaluate soluble cation release, quantity and identity of corrosion products, as well as interrogate the role of Al on the chemical, structural, and electronic defect structure of oxides formed. Al became captured in Cu_2O as a substitutional cation defect which in turn caused structural, and electronic modifications. This doped film did not inhibit soluble Cu cation release for antimicrobial function even after 144 h. Al-doped cuprous oxide had fewer electronic charge carriers (holes) due to Al-doping and subsequent increased electronic resistance. These results are promising regarding the aim of generating a tunable tarnish-resistant layer for an antimicrobial Cu-based alloy.
© The Author(s) 2018. Published by ECS. This is an open access article distributed under the terms of the Creative Commons Attribution 4.0 License (CC BY, http://creativecommons.org/licenses/by/4.0/), which permits unrestricted reuse of the work in any medium, provided the original work is properly cited. [DOI: 10.1149/2.1301810jes]

Manuscript submitted May 4, 2018; revised manuscript received July 23, 2018. Published August 4, 2018.

Motivation.—Cu and some of its alloys have demonstrated the ability to kill antibiotic-resistant so-called 'superbugs' on contact within minutes.[1–3] Hospital-acquired patient infections are becoming an increasingly difficult battle worldwide: a battle which we humans are losing.[4–7] In response, many pharmaceutical companies have significantly reduced future development of antibiotics to combat these multi-drug resistant pathogens due to increased pandrug-resistance.[4] Novel infection control methods are needed to prevent the spread of infection and subsequent deaths of those individuals infected. Cu and its alloys show promise in this regard as antimicrobial high-touch surfaces; targeting the most common transmission vector (hand contact) with a functional antimicrobial alloy.[2,6,8] However, Cu and its alloys tend to tarnish, and this tarnishing layer (patina) can be unaesthetic as a commonly touched surface. Thin passive oxide layers inhibit the corrosion needed to provide soluble Cu ions which are needed for this antimicrobial function.[9] A representative electrolyte solution is needed to appropriately simulate a high-touch surface, such as artificial perspiration. An ideal alloy would be tarnish-resistant but not completely passive, for both aesthetic and functional reasons, yet permit enough soluble Cu to be released through corrosion to facilitate continuous antimicrobial function. In this aim, a solid solution alloy of Cu with Al is a good candidate for a tarnish-resistant antimicrobial alloy.

Tuning of the corrosion layer electronic properties has been demonstrated with Ni in cupro-nickel alloys. Ni in solid solution Cu-Ni and Cu-Al-Ni enhances alloy corrosion resistance by incorporation of Ni^{2+} into Cu_2O replacing the Cu^+ cation vacancies with a cation of greater valence, doping the oxide and decreasing the number of electronic charge carriers (e^- holes) and thus the conductivity of the oxide.[10] This effect increases with increasing Ni content up to 30% Ni.[11,12] However, Ni is a common metal allergen[13] and would therefore be unsuitable for an antimicrobial high-touch alloy. Altering the properties of the cuprous oxide layer may also be possible using Al, provided the alloying content is below the passive threshold. An exotic opportunity may exist to generate a tunable alloy by doping the cuprous oxide with an aliovalent solute such as Ni^{2+} or Al^{3+}, modifying the ionic and electronic properties of the cuprous oxide layer with the aim of mitigating corrosion of the alloy. Cu-Al alloys show remarkable corrosion resistance[14,15] with excellent mechanical performance,[16–18] making this alloy system an attractive material in pumps, impellers and valves exposed to seawater[11,19,20] and dental alloys.[15,21] Alternatively, surface coverage of a corrosion-limiting film may be tunable by controlling the alloy content of Al in solid solution to prevent passivity but permit an allowable amount of soluble Cu release through corrosion. Unlike Ni^{2+} however, Al^{3+} is not thermodynamically soluble in Cu_2O and may oxidize in another form, such as a separate oxide (e.g., Al_2O_3) or dissolve into solution.

Possible Fates of Al Following Corrosion

Following corrosion of the Cu-Al alloy, Al may terminate in one of many 'fates': release as a soluble aqueous ion, as a stoichiometric or mixed oxide phase, or incorporated in a copper corrosion product. Table I lists the thermodynamic free energies of the solid compounds predicted to form from a Cu-Al alloy in aqueous environment; they are ranked in order of increasing stability (more negative free energy). The role of Al on the corrosion of Cu-Al alloys is dependent on where the Al resides following oxidation, i.e. its 'fate'. A few probable scenarios as to the fate of the alloy are discussed.

Phase segregated stoichiometric oxides – $Cu_2O + Al_2O_3$.—Cu-Al alloys are argued to be protected from corrosion by a thin alumina (Al_2O_3) layer.[16] Some research purports[16,22–24] that a duplex layer of Cu_2O and Al_2O_3 coexist on the surface, and that the alumina phase is responsible for the corrosion protection of the alloy.[16,22,23] The increased corrosion protection with increasing Al content is purportedly due to increased surface coverage (site blocking) of transport of Cu^+ at the interface of this oxide.

Cu-Al mixed oxide phases.—Another potential fate of Al is in the form of a distinct oxide with copper. Copper, aluminum, and oxygen together may form thermodynamically stable copper aluminate phases. Sanderson and Scully observed copper aluminate phases in high temperature corrosion studies of Al-bronze alloys[25] however, there is a paucity of evidence regarding these phases in the oxide following oxidation in aqueous environments. Electrochemical thermodynamics predicts these mixed phases are the most stable (Table I) and predominant phases in neutral aqueous solutions.[26] The corrosion product formed on the surface of corroded Cu-Al in artificial perspiration may form $CuAlO_2$ or a $CuAl_2O_4$ spinel phase.

Solute capture of Al^{3+} in Cu_2O.—A third possibility exists, that the solute elements may become captured in the growing oxide layer

*Electrochemical Society Student Member.
**Electrochemical Society Fellow.
[z]E-mail: mjh3aj@virginia.edu

Downloaded on 2018-10-27 to IP 165.124.166.111 address. Redistribution subject to ECS terms of use (see ecsdl.org/site/terms_use) unless CC License in place (see abstract).

Table I. Selected Gibbs Free Energies of Oxidized Cu and Al Compounds.[26,53]

Compound Name		ΔG^0_{298} (kJ/mol)
CuCl	Nantokite	−119.7
CuO	Tenorite	−127.9
Cu_2O	Cuprite	−147.9
$CuCl_2 \bullet 2H_2O$	Eriochalcite	−655.9
$CuAlO_2$	Copper Aluminate	−868.6
$Cu_2(OH)_3Cl$	Botallackite	−1322.6
$Cu_2(OH)_3Cl$	Atacamite	−1339.2
$Cu_2(OH)_3Cl$	Clinoatacamite	−1341.8
Al_2O_3	Alumina	−1581.4
$CuAl_2O_4$	Copper Aluminate	−1695.1

to form a metastable phase containing Al^{3+} in a Cu_2O solid solution. Should the interface velocity of the oxidation front exceed the velocity of the solute diffusional transport perpendicular to the interface then a separate segregated oxide is restricted from forming and solutes such as Al^{3+} are captured in the growing Cu_2O oxide.[27] This metastable oxide then becomes doped with an aliovalent ion and would have significant effects on the electronic properties of the oxide film with subsequent effects on the corrosion of the alloy.[28]

Aluminum as a solid solution addition may afford corrosion protection to Cu-Al alloys by one of several mechanisms: Al may oxidize as a separate Al_2O_3 phase, a mixed oxide such as $CuAlO_2$ or a $CuAl_2O_4$, or as a dopant substitutional cation in Cu_2O. In this aim, high-purity single phase FCC model binary copper alloys buttons of various Al content were fabricated for study. Corrosion rates, electrochemical behavior, oxide identity and quantity, and soluble Cu release were measured in artificial perspiration to simulate the high-touch environment. Specifically, the chemical and structural nature of the tarnish-resistant oxides formed on the surface of Cu-Al alloys was determined with surface analytical techniques and X-ray diffraction. Furthermore, an estimate of the charge carrier density of the semiconducting oxide was determined to assess the effect of doping (if any).

The objective of this work is to determine the role of Al on the tarnish-resistance of Cu-Al alloys in the aim of generating a tarnish-resistant oxide which does not inhibit Cu ion release in order to enable antimicrobial function.

Experimental

Materials.—*Alloy preparation.*—High-purity binary alloys of Cu-Al were prepared by inert-gas (argon) arc-melting. Al concentrations of 0.2, 2, and 11 at% (0.1, 1, and 5 wt%) were prepared from a minimum 99.99 wt% pure Cu and Al materials. Alloy contents are reported in at% unless otherwise indicated. The alloy buttons were melted and flipped three times to homogenize. The actual chemical compositions are given in Table II as tested by ASTM E478. Alloy buttons were heated to 600°C for 2 h to solutionize and quenched in water. Solid solution was confirmed with X-ray diffraction by a single Cu FCC diffraction pattern with shifted peaks due to Al in solid solution. Prior to electrolyte solution exposure or electrochemical experiments, alloy samples were ground with SiC polishing paper up to 1200 grit, the final polishing stage was lubricated with ethanol. After polishing, samples were rinsed with and then immersed in ethanol, dried with compressed lab air and transferred to sample cells within 30 min for electrochemical testing or exposure. For improved visual inspection and photoelectron studies, samples were polished through 1-μm diamond suspension and rinsed with ethanol. However, air aging was identical.

Table II. Elemental composition (wt%) of commercial-grade Cu, Al, and high-purity custom binary Cu-Al alloys as tested according to ASTM E478.

Alloy	Cu/wt%	Al/wt%	Other/wt%
Cu	99.997	–	–
Cu-0.2Al	99.91	0.09	–
Cu-2Al	99.01	0.99	–
Cu-11Al	95.22	4.78	–
Al	00.06	99.38	0.37 Fe, 0.13 Si, 0.02 Ga

Table III. Chemical composition of artificial perspiration solution (pH 6.50 ± 0.05) based on B.S. EN1811.[32]

Chemical Name	g/L	Molarity (mM)
NaCl – Sodium Chloride	5.00	85.6
CH_4N_2O - Urea	1.00	16.7
$C_3H_6O_3$ - L(+) Lactic Acid (90%)	1.00	11.1
NH_4OH –Ammonium Hydroxide	pH Adjuster	∼11

Electrolyte solutions.—*Artificial perspiration.*—Artificial perspiration was used to represent a high-touch surface[9,29–31] and prepared according to BS EN 1811:2011.[32] The chemical composition of artificial perspiration is given in Table III. The pH was adjusted with ammonium hydroxide (NH_4OH). The pH of the artificial perspiration drifted from 6.5 to 5.8 over the course of 10 days therefore, the artificial perspiration was prepared and pH-adjusted within 6 h before sample exposure.

Borate buffer.—Galvanostatic cathodic coulometric reductions (CR) to assess Cu oxides were performed in a deaerated borate buffer solution (pH 8.4). This buffer to fix pH was prepared from 0.11 M boric acid (H_3BO_3) and 0.02 M sodium tetraborate ($Na_2B_4O_7$). Deaeration of the solution was accomplished by bubbling N_2 gas through a glass fritted bubbler for a minimum of 1 h and hydraulically transferred to a N_2-purged cell to prevent electrolyte exposure to lab air in identical fashion as has been described in detail elsewhere.[9,29,30]

Characterization of corrosion products formed on Cu-Al at open circuit in artificial perspiration.—Open circuit exposures were conducted in 300 mL 3-electrode cells. Exposed sample area through a rubber O-ring was 0.8 cm^2. Cell bodies were cleaned using 0.1 M HCl solution prior to each exposure, rinsed with distilled water and rinsed with the respective electrolyte solution. Potentials were measured with a saturated calomel electrode with a Luggin probe tip. Optical photographs were measured with a flatbed digital document scanner with a grey-card color reference background at a resolution of 300 DPI.

An InVia Renishaw Raman spectrometer acquired Raman spectra generated from the green emission line of an Argon laser (514 nm) with a 3000 l/mm diffraction grating with a Peltier-cooled CCD detector. Raman spectroscopy was measured on samples exposed to artificial perspiration for 96 h. Burning of the sample surface was avoided by using longer exposure times (∼minutes) with lower laser powers.

Crystal diffraction patterns from the corrosion product films were measured using a grazing-incidence method. The incident angle gave optimal signal-to-noise at a value of $\omega = 0.5°$. Full penetration through the corrosion product film to the alloy substrate was achieved as evidenced by FCC peaks of the substrate matching those measured from solid solution confirmation results via bulk crystal X-ray diffraction.

The elemental composition, chemical state, and variations through the thickness of the oxide film was evaluated with X-ray photoelectron spectroscopy (XPS). A Thermoscientific K-Alpha XPS instrument used a monochromatic Al K_α X-ray source (1486.6 eV). Photoelectron (PE) spectra were obtained on samples exposed to artificial perspiration for 96 h. PE spectra were acquired on the as-introduced samples as well as sputtered by Ar^+ ions lightly, and at several sputtered depths to the metal substrate. An Ar^+ ion beam energy of 3 keV was used which corresponded to a sputter rate of 0.3 nm/s using a SiO_2 sample of known thickness. Spectral fits were accomplished

Downloaded on 2018-10-27 to IP 165.124.166.111 address. Redistribution subject to ECS terms of use (see ecsdl.org/site/terms_use) unless CC License in place (see abstract).

using standard fit constraints.[33] The Al 2p peak was resolved by fitting a third peak after constraining the software peak fit of the Cu 3p spit-obit energy split ($\Delta = 2.0$ eV) and the relative peak area ratios (1:2). For the X-ray generated Auger transition, the main line was determined from spectra fits using the least number of components peaks which gave reasonable agreement with the data (STD < 2).

The concentration of a given element from the integrated element peak area was calculated using standard methodologies.[33] The concentration (C_x) of a given element from the PE spectra is given by Equation 1.

$$C_x = \frac{\frac{I_x}{S_x}}{\sum_i \frac{I_i}{S_i}} \quad [1]$$

Where I_x is the integrated peak intensity of element x, and the atomic sensitivity factors (S) used were 5.321 for Cu, 0.234 for Al, 0.711 for O, and 0.891 for Cl, taken from Ref. 33.

The charge carrier density of the cuprous oxide (cuprite, Cu_2O) is possibly responsible for the change in electrochemical behavior of these alloys. To determine the electronic/ionic defect density of the oxide, Mott-Schottky experiments were performed in solutions of deaerated borate buffer (pH 8.4) with 0.7 mM of $K_3[Fe(CN)_6]$ as a redox mediator.[34] Oxide films were grown in quiescently-aerated artificial perspiration with an anodic galvanostatic hold at 0.1 mA for 12500 s over an exposed electrode are of 0.8 cm^2. Following sample transfer to deaerated cells, a cathodic sweep was applied to samples starting at 0 V_{MMSE} at a rate of 5 mV/s with an applied AC voltage of 5 mV RMS at a frequency of 10 Hz. The frequency selection rationale was to use the highest frequency possible to avoid leakage currents and electronic transitions as well as avoid growth or dissolution of the oxide but yet remain sufficiently close to the characteristic frequencies of the oxide space charge capacitance. 10 Hz was found experimentally to be the optimal frequency for this measurement; higher frequencies were attempted but were in the solution resistance region and were not successful. Deaeration and the use of a redox mediator also help prevent changes in the thickness of the oxide layer via oxidation or reduction. Electrode potentials were measured using a mercury/mercurous sulfate electrode (MMSE). The charge carrier density can be approximated with the Mott-Schottky equation reproduced in Equation 2.

$$\frac{1}{C^2} = \frac{2}{\varepsilon\varepsilon_0 A^2 e N_d}\left(E - E_{fb}\right) \quad [2]$$

Where C is the measured differential capacitance, ε_0 is the permittivity of free space (8.85×10^{-14} F/cm), ε is the dielectic constant of the oxide (7.6),[35] A is the electrode area (0.8 cm^2), e is the elementary charge (1.6×10^{-19} C), and N_d is the defect density. E and E_{FB} are the electrode potential and the flatband potential of the semiconducting oxide, respectively. The defect density can thus be estimated from the slope of the $1/C^2$ vs. potential plot. The use of a redox mediator ensures that the majority of the faradaic charge is consumed by the mediator rather than oxidation or reduction of the oxide. Electrochemically-grown oxides violate the assumptions of the ideal conditions of which the Mott-Schottky equation is derived[a] thus,[36] the precise concentration of charge carriers cannot be obtained. However, it is nonetheless instructive to compare the approximate relative defect density values between oxides formed on Cu-Al alloys with differing Al contents.

Anodic charge of corrosion products.—*Insoluble corrosion products – coulometric reduction.*—The reversible Nernst potentials for copper corrosion products usually lie within the electrochemical stability window of water (−0.5 to 0.7 V_{SHE} at pH 8.4), in the absence of dissolved oxygen, these compounds can be galvanostatically reduced in aqueous electrolytes. A constant cathodic current of −20 μA was applied (A = 0.8 cm^2, −25 μA/cm^2) to pre-exposed samples in a deaerated aforementioned borate buffer solution (pH 8.4). Deaerated solution was hydraulically transferred to reduction cells. Reduction cells (~400 mL total volume) were N_2-purged for 10 min prior to direct electrolyte transfer from the deaeration flask. Continuous bubbling of reduction cells ensured deaeration throughout the reduction. Reduction potentials were measured using a mercury/mercurous sulfate electrode (MMSE) fitted with Luggin tips. The charge of the oxide can be determined from the chronopotential curve via the following relation (Equation 3).

$$Q_{CR} = i_{app} \times t_{red} \quad [3]$$

Where i_{app} is the applied current density (−25 μA/cm^2) and t_{red} is the reduction time, determined as time between local maximum potential changes, i.e. distance (time) between maxima in the first derivative plots of chronopotential curves according to procedures outlined in detail in previous work.[29,30,37] The thickness of the oxide can be roughly estimated through the calculation in Equation 4.

$$d = \frac{Q_{CR}(MW)}{nF\rho} \quad [4]$$

Where d is the corrosion product thickness in cm, Q_{CR} is the charge density associated with a reduction wave (Coul/cm^2), MW is the molecular weight of the oxide (g/mole), n is the number of moles of e^- per mole of oxide molecule (e.g., $Cu_2O = 2$), F is Faraday's constant, and ρ is the oxide density in g/cm^2. Cu_2O density was assumed to be 6.0 g/cm^3.

Soluble corrosion products – ICP-OES.—Soluble metal ion concentration was measured using inductively-coupled plasma (T ≥ 6000 K) – optical emission spectroscopy. A Thermoscientific iCap 6000 spectrophotometer was used to collect photoemission spectra from aliquots (15 mL) obtained from cells with 300 mL (± 2.5 mL) of artificial perspiration solution (not acidified). As a control study and to determine the valence of soluble Cu for the present and other work: stronger chelators such as citric acid (log ß = 5.8 vs. lactic acid: log ß = 2.7) have shown excellent quantified dose-response to galvanostatic anodic holds and measured ion release and oxide quantity via unacidified ICP.[9,29,30,37–39] Emission intensities were compared with calibrated standards of known concentrations. LOD were found to be 17 and 198 ppb for Cu and Al, respectively. The chemical species from the artificial perspiration solution gave a high background noise for even the acidified standards measurement of Al. Studies with Nordic gold (Cu-5Zn-5Al-1Sn) investigated the potential for Al release (with acidified and unacidified samples) with far greater corrosion rates (x2) and showed no detectable Al release (lowest standard used = 0.01 ppm) in artificial perspiration.[9] Yet in the present work with a pure Al sample, there were significant amounts of soluble Al (0.8 ppm) detected by this methodology using unacidified artificial perspiration (discussed in later sections). The measured concentration can be converted to an equivalent charge through the following expression.

$$Q_{ICP} = \sum \frac{CVnF}{AW} \quad [5]$$

Where C is the measured concentration (mg/L), V is the solution volume (L), n is the assumed valence state of the soluble ion, F is Faraday's constant (Coul/mole e^-), and AW is the atomic weight of the element of interest (mg/mole). Prior work identified that soluble Cu was in the cuprous state.[30,38]

Total anodic charge – corrosion rates in artificial perspiration.—*Gravimetric mass loss.*—Gravimetric mass loss (ASTM-G1)[40] was used to determine the total corrosion loss from Cu-Al alloy samples exposed to artificial perspiration up to 96 h. Triplicate measurements of samples before (M_1), and after (M_2) exposures were compared with the measured values of samples cleaned of corrosion products using a 6 M HCl solution in one cycle lasting 1–2 minutes (M_3). A 0 h sample

[a]Electrochemically grown oxides are highly defective and contain localized states in the bandgap with a wide range of energies. These localized states have various time constants leading to a frequency dependence of the space charge capacity.[36] In the present work we only use Mott-Schottky to compare the relative difference between alloy systems without conferring absolute values to the charge carrier densities.

Downloaded on 2018-10-27 to IP 165.124.166.111 address. Redistribution subject to ECS terms of use (see ecsdl.org/site/terms_use) unless CC License in place (see abstract).

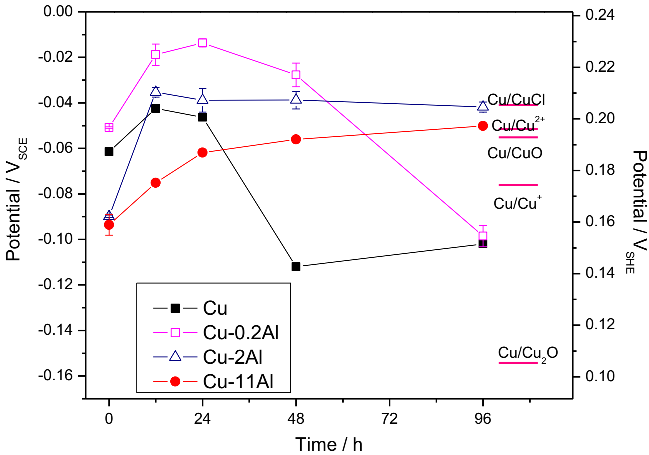

Figure 1. Open circuit potential of Cu, Al, and Cu-Al alloys in quiescently-aerated artificial perspiration over time up to 96 hours. Selected Nernst potentials of interest are also shown on plot. Al sample OCP = -0.55 V_{SCE} not visible on this scale. Al→Al_2O_3 $E_r = -2.2$ V_{SCE}.

with no other exposure was included to show the mass loss from the acid cleaning step alone. The total mass loss was the difference between M_1 and M_3. The mass loss was estimated using a faradaic relation with the assumed equivalent weights of 63.6, 63.2, 59.9, 48.8, 41.1, and 9.0 g/equivalent for Cu, Cu-0.2Al, Cu-2Al, Cu-11Al, and Al, respectively.

Electrochemical interface - EIS.—Electrochemical impedance spectroscopy was measured on samples at set interval time points up to 96 h. A 30-min open circuit measurement was taken prior to obtaining EIS spectra. The frequencies applied ranged from 100 kHz to 1 mHz with 8 points per decade. The voltage perturbation applied was 10 mHz RMS. A DC equivalent circuit of two constant phase elements each in parallel with resistors both in series with a solution resistance was used to mathematically approximate the impedance-response of samples and determine the polarization resistance (R_p) value, defined as the impedance at the DC-limit (freq. → 0) under AC conditions. Gamry software was employed to calculate circuit values using a non-linear regression analysis. The integrated B/Rp ($\sim i_{corr}$) values gave an indication of the total anodic charge Q_{EIS} for corrosion analogous to the charge estimated from mass loss. The total anodic charge integrated from impedance-derived polarization was calculated according to Equation 6.

$$Q_{EIS} = \int_0^t \frac{B}{R_p} dt \quad [6]$$

Where B is the Stern-Geary constant (B = 0.025 V)[9,29,30] ($b_a b_b/(b_a+b_b)$), R_p is the polarization resistance of the system ($R_{ox}+R_{ct}$), and t is time duration of the sample in artificial perspiration. Integrating the R_p values fit from impedance spectra over the time intervals measured gives an approximate value of the total anodic charge from corrosion over time. The total anodic charge is analogous to the cumulative material loss measured via mass loss and agrees well with the trend where Cu-2Al demonstrated the greatest total anodic charge.

Potentiodynamic polarization.—Potentiodynamic polarization scans from -1.5 V_{SCE} to 0.5 V_{SCE} were conducted on freshly polished Cu-Al samples in ambiently-aerated artificial perspiration and 1 M HCl at an upward scan rate of +0.1667 mV/s. Prior to polarization scans samples were held at -1.5 V_{SCE} for 10 minutes to remove any air-formed oxides on the surface.

Results

Characterization of corrosion products formed on Cu-Al in artificial perspiration.—Open circuit potentials of Cu, Cu-Al, and Al in artificial perspiration were monitored over time and presented in Figure 1. A clear delineation between alloys with 2 at% Al or greater is shown at 96 h. Potentials remain high (-40 mV_{SCE}) for 2 at% Al or greater alloys, but the potential falls to a lower value (-100 mV_{SCE}) after 24 h for pure Cu and 48 h for Cu-0.2Al in artificial perspiration solution. The Cu-11Al alloy rises slowly, suggestive of an increasing resistive or thickening film, but reaches a similar OCP value to Cu-2Al at 96 h. The surface of Cu-Al samples became tarnished with corrosion products as shown in Figure 2. Cu-Al samples at 2 at% or lower showed oxide tarnish similar in nature to pure Cu. However, Cu-11Al showed far less tarnishing oxide and some light etching of the grain boundaries (Figure 2).

Ex situ Raman spectroscopy, presented in Figure 3, identified cuprite (Cu_2O) as a corrosion product formed on all Cu-Al alloys tested following exposure to artificial perspiration. Raman spectra acquired on a pure Al sample, also exposed in artificial perspiration for 96 h, showed distinctly different Raman peaks, particularly its main broad peak centered at 785 cm^{-1}, which were not observed in the Raman spectra on the Cu-Al samples or on the corundum (Al_2O_3) reference spectra.[41] Notably, an additional Raman band not on the cuprite standard but found on all Cu-based corroded samples at 525 cm^{-1} which has been ascribed to Cu-OH vibrations which would indicate a defective cuprite (Cu_2O) structure.[42] In summary, Raman spectroscopy only revealed defective Cu_2O but did not reveal any independent phase of oxidized aluminum (Al_2O_3) or mixed metal oxide phases (e.g., $CuAlO_2$) on Cu-Al alloys.

Crystalline corrosion products on the surface were characterized using grazing-incidence X-ray diffraction (GIXRD) and diffraction patterns with corrosion product assignments are presented in Figure 4. Cuprite (Cu_2O) was found with evidence (one peak) of CuCl. The assignment of cuprite with this singular peak has been previously identified as CuCl in prior work.[30] All diffraction peaks were identified and were also indicated from evidence from other methods (Raman: Figure 3, CR: Figure 9, XPS: Figure 6). Complete penetration to the substrate was achieved, evidenced by the Cu FCC peaks albeit shifted for each alloy due to Al in solid solution (Figure 4). Dealloying may be indicated with GIXRD by a shift or separation of Cu FCC lattice peaks which would occur in the case of pure Cu FCC peaks (or possibly shoulder peaks) neither of which were observed here. For the Cu-11Al sample, the cuprite (111) peak was slightly shifted to higher

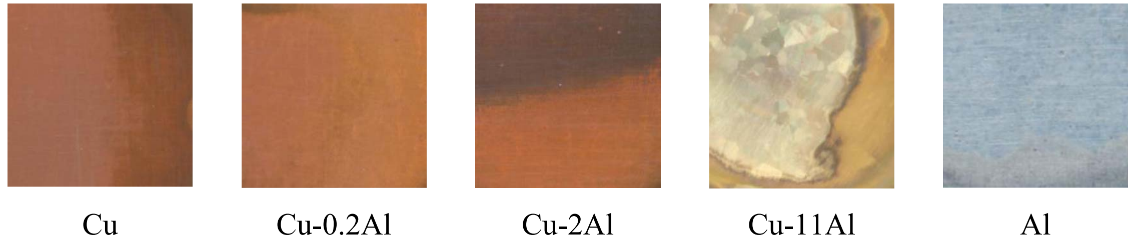

Figure 2. Visual surface condition of Cu-Al alloys following full immersion exposure to artificial perspiration for 96 h. Horizontal dimension is 5 mm.

Downloaded on 2018-10-27 to IP 165.124.166.111 address. Redistribution subject to ECS terms of use (see ecsdl.org/site/terms_use) unless CC License in place (see abstract).

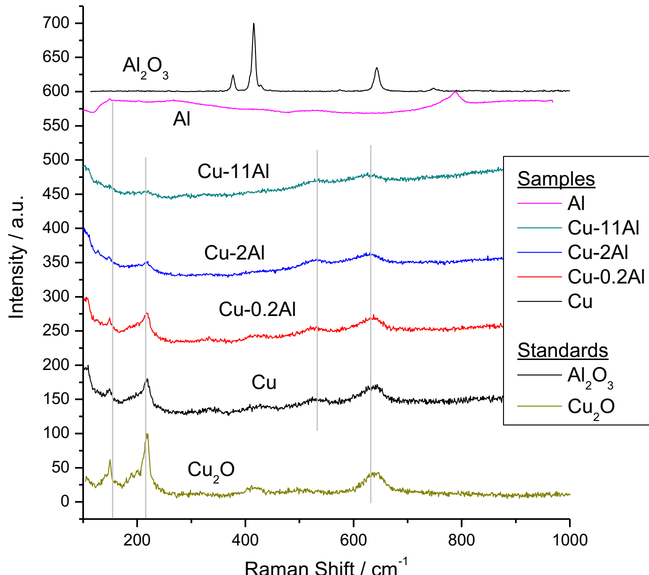

Figure 3. Raman spectroscopy of Cu, Al, Cu-Al samples, and standard reference cold-pressed powder pellets of suspected corrosion products Cu_2O and Al_2O_3.

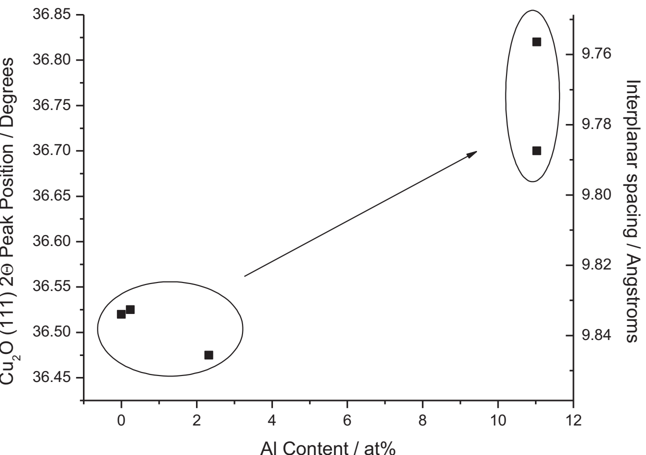

Figure 5. Peak position, 2Θ, of the (111) Cu_2O lattice and approximate interplanar spacing as a function of Al content.

2Θ values (Figure 4), indicative of Al^{3+} in Cu_2O. The full width at half maximum (FWHM) of this diffraction peak increases, indicating less structural uniformity of this corrosion product.[43] A decrease in the peak height of cuprite is also observed with increasing Al content in the alloy shown in Figure 4. Not only does the thickness of the oxide decrease with increasing Al content, the cuprous oxide on the alloy surface attains a slightly different lattice parameter, evidenced by the shift in the (111) reflection according to Bragg's law demonstrated in Figure 5.

High-resolution photoelectron spectra for selected elements measured from corroded Cu-11Al are given in Figure 6. A summary of the photoelectron peak fit values and computed areas are given in Table IV. Al 2p photoelectron energy overlaps with Cu 3p energies. However, by imposing typical fitting constraints on Cu 3p peaks, the Al 2p signal was resolved from the spectra in the case of the Cu-11Al (Figure 6a) and Cu-2Al alloys. The Al 2p energy (73.17 eV) was consistent with an oxidized state, but did not agree with values expected for Al_2O_3 or $Al(OH)_3$ (73.9 and 74.0 eV, respectively).[33] O 1 s spectra show two clearly resolved peaks (Figure 6b). The first peak (530.27 eV) matches clearly with the expected value for Cu_2O (530.3 eV), while the second (531.11 eV) is more closely related to Al-O bonding in Al_2O_3 (531.0 eV). However, the binding energy was also close to that of $Cu(OH)_2$ (531.2 eV). Al was oxidized as inferred from its 2p spectra and the O 1s peak. This assignment is not entirely conclusive on its own due to the reasons previously mentioned and the confirmed presence of OH from Raman spectra. The Cu 2p energy does not shift appreciably from Cu(I) to Cu(0), therefore, the Auger Cu_{LMM} transition energy shown in Figure 6c was used to delineate the oxide Cu_2O: (Cu(I): 916.7 eV)/alloy (Cu(0): (918.6 eV) boundary. The chlorine peak energy ($2p_{3/2}$ = 198.64 eV, Figure 6d) was consistent with well-established energy ranges for chlorine binding in CuCl (198.4–199.5 eV).[33] The cation fractions of Al in the film are discussed in a later section (§ The Fate of Al Following Corrosion in Artificial Perspiration: Solute Capture). In summary, the primary corrosion products identified were oxidized Al (though not definitively

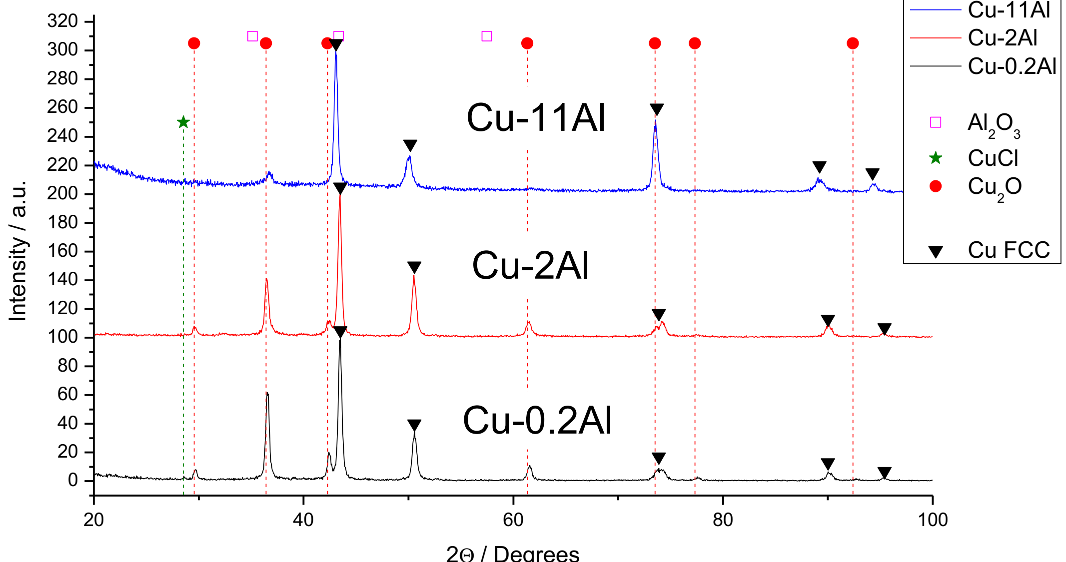

Figure 4. Grazing-incidence X-ray diffraction patterns of Cu-Al samples following 96 h at open circuit in artificial perspiration. The incident angle, ω, was set to 0.5° to limit the illumination depth. Alloy substrate assignments account for 2Θ displacement from solid solution alloying.

Downloaded on 2018-10-27 to IP 165.124.166.111 address. Redistribution subject to ECS terms of use (see ecsdl.org/site/terms_use) unless CC License in place (see abstract).

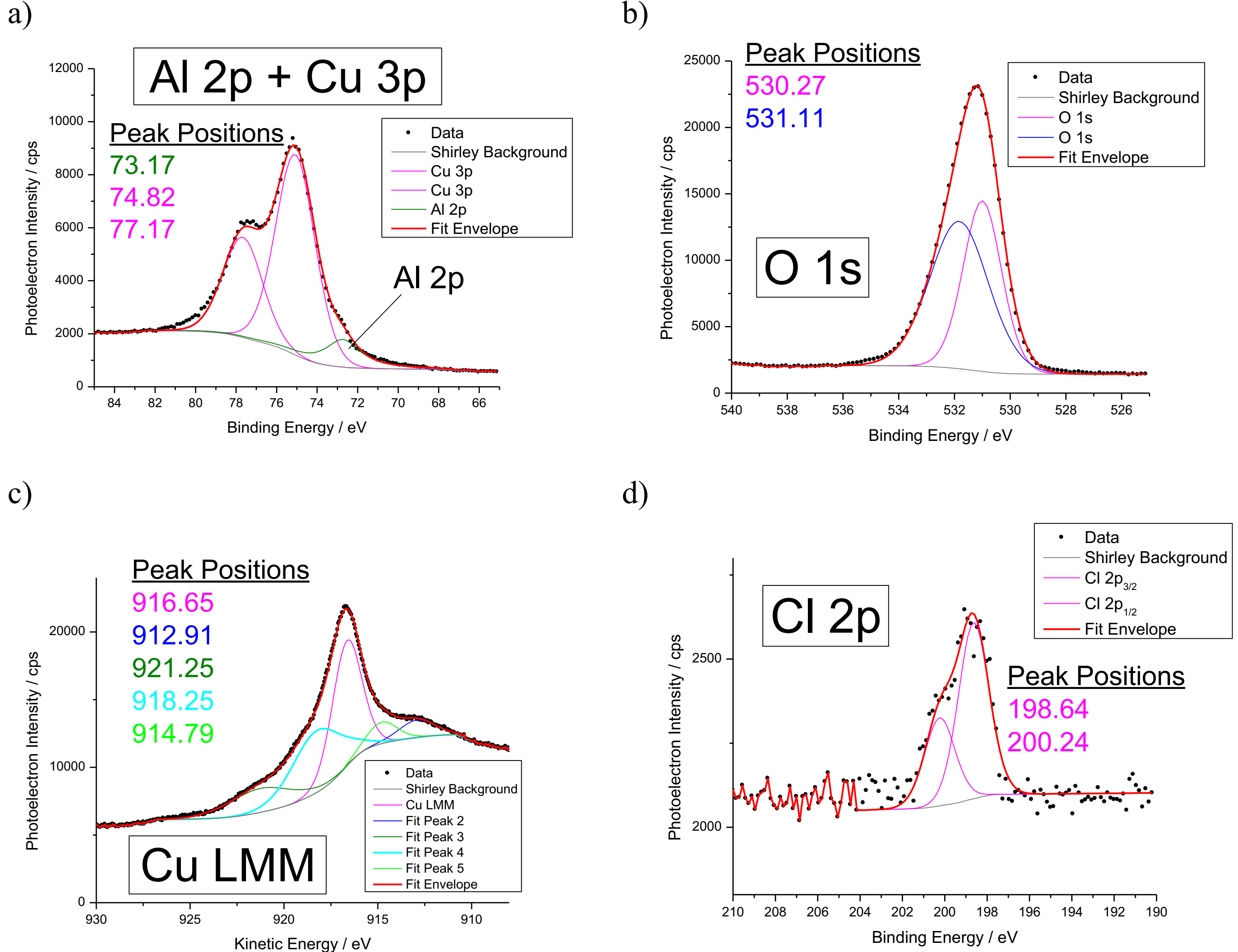

Figure 6. High resolution X-Ray photoelectron spectra of the as-introduced sample of Cu-11Al following 96 h of full-immersion exposure to artificial perspiration at open circuit. (a) Aluminum 2p and Copper 3p, (b) Oxygen 1s, (c) Cu LMM Auger transition, and (d) Chloride 2p. Photoelectron energies were calibrated using the Au $4f_{7/2}$ peak set to 84.0 eV.

Al_2O_3 or $Al(OH)_3$), Cu_2O with Cl^- embedded in the cuprite, and possibly also as a separate phase of CuCl on the surface.

Cuprous and cupric oxides are both p-type semiconductors, whereas aluminum oxides are n-type. Mott-Schottky measurements (Figures 7a–7d) made on galvanostatically-grown oxide films indicate p-type semiconducting properties (Figure 7c). The impedance spectra of Cu-Al alloys artificial perspiration solution are given in Figures 7a and 7b. The estimated values of electronic defect densities of oxides formed on Cu-Al alloys in sweat are presented in Figure 7d. Estimated defect densities revealed relatively decreased electronic charge carriers, i.e. electron holes, in the cuprous oxide formed on Cu-11Al samples compared with the defect density values measured for Cu, Cu-0.2Al and Cu-2Al.

Anodic charge of corrosion products.—*Insoluble corrosion products – coulometric reduction.*—The coulometric methodology utilized and corrosion product assignment procedure has been discussed in detail in a prior publication.[30] The electrochemical nature and amounts of the corrosion products formed were quite different as a function of Al content as shown in Figure 8 based on reduction on Cu-Al samples following exposure in artificial perspiration at open circuit. Coulometric reductions show a markedly decreased charge associated with cuprous oxide with increasing Al alloying content. Al is not reducible with this technique; its reduction potential is far below that of HER. Greater amounts of CuCl are found on Cu-2Al compared to Cu-0.2Al and Cu-11Al (Figure 9). A general trend of decreased cuprite (Cu_2O) thickness with increasing Al content in the alloy is shown with triplicate measurements in Figure 9.

Figure 9 illustrates the progression of data processing from the coulometric reduction method. Separate replicate samples showed good reproducibility in coulometric reduction following full immersion for 96 h in artificial perspiration at open circuit demonstrated by their chronopotential plots in Figure 9a. Only two corrosion products were identified (via reduction potential) with this method, indicated by the outlined areas in Figure 9b. CuCl and Cu_2O were electrochemically reduced from Cu-0.2Al and Cu-2Al samples, but only Cu_2O was electrochemically reduced on Cu-11Al (Figures 9b and 9d). The reduction potential for cuprite (Figures 9b) was found to decrease by 100 mV from Cu to Cu-11Al, meaning the cuprous oxide formed on Cu-11Al was more difficult to reduce than the Cu_2O formed on the solute-lean compositions. The modified reduction potential and lattice structure (Figures 4 and 9b) are unlikely to simply be an effect of the thin oxide itself. The air-formed oxide on the surface reduces at a higher potential, inferring the thin oxide is easier to reduce rather than more difficult. Secondly, the reduction potential for the oxide changes with alloy content (Figure 9b) to a far greater degree than over exposure time or oxide thickness. Reducible copper corrosion products significantly decreased in thickness (reducible amounts measured as

Downloaded on 2018-10-27 to IP 165.124.166.111 address. Redistribution subject to ECS terms of use (see ecsdl.org/site/terms_use) unless CC License in place (see abstract).

Downloaded on 2018-10-27 to IP 165.124.166.111 address. Redistribution subject to ECS terms of use (see ecsdl.org/site/terms_use) unless CC License in place (see abstract).

Table IV. Spectra fitted peak values and areas of XPS and X-ray-induced Auger electron data of Cu-Al alloys exposed to artificial perspiration for 96 h at open circuit. Sputtering rate was measured as 0.3 nm/s on a SiO_2 sample.

		Al_{2p}		O_{1s}		Cu_{2p}		Cu_{3p}		Cu_{LMM}	Cl_{2p}	
Sputter Time (s)		Peaks (eV)	Area	Peaks (eV)	Areas	Peaks (eV)	Areas	Peaks (eV)	Areas	Peaks (eV)	Peaks (eV)	Areas
Cu-0.2Al	0	-	-	530.49, 531.05	7883, 8059	932.56, 952.36	145844, 72922	77.56, 75.09	71212, 17700	916.41	198.65, 200.25	1830, 915
	350	-	-	530.39, 530.03	8861, 3377	932.55, 952.35	232191, 116096	77.59, 75.11	8894, 22820	916.71	199.07, 200.67	1123, 562
	700	-	-	530.32, 529.49	1194, 351	932.62, 952.42	2374112, 118706	77.53, 75.06	9344, 23389	918.64	199.31, 200.91	72, 36
	1750	-	-	529.76, 530.43	66, 128	932.62, 952.42	232387, 116193	77.53, 75.06	8919, 22908	918.83	-	-
Cu-2Al	0	71.91	522	530.26, 531.47	13529, 6374	932.34, 952.14	125476, 62738	77.32, 74.87	7630, 15597	916.68	198.28, 199.88	1083, 541
	350	-	-	530.34, 531.60	673, 585	932.63, 952.43	339515, 169757	77.46, 74.99	13592, 30433	918.68	-	-
	700	-	-	530.39, 531.73	321, 253	932.64, 952.44	340837, 170418	77.46, 75.00	13014, 30935	918.66	-	-
	1750	-	-	530.90	653	932.64, 952.44	338932, 169466	77.47, 75.01	12767, 31181	918.67	-	-
Cu-11Al	0	73.17	3921	530.27, 531.11	5854, 17096	932.33, 952.13	8428, 42140	77.17, 74.82	8791, 9944	916.65	198.64, 200.24	969, 485
	375	71.26	472	531.00, 531.83	22591, 29856	932.84, 952.64	48922, 24461	77.74, 74.84	4626, 12347	918.38	198.97, 200.57	586, 2923
	750	72.72	3484	530.96, 531.75	10626, 10590	932.78, 952.58	228817, 114409	77.67, 75.07	9411, 18822	918.62	199.03, 200.63	221, 111
	1125	73.00	6718	530.96, 531.88	30153, 427	932.71, 952.51	298279, 149140	77.38, 75.03	14643, 17856	918.61	-	
	1500	73.05	7880	530.66, 531.75	362, 1897	932.72, 952.52	326038, 163019	77.35, 75.05	16902, 17950	918.61	-	

Figure 7. Electrochemical impedance spectra Bode magnitude (a) and phase (b) of Cu-Al alloys for 96 hours artificial perspiration. Measurements of galvanostatically pre-grown oxide films (see § Characterization of Corrosion Products Formed on Cu-Al at Open Circuit in Artificial Perspiration) on Cu-Al alloys using the Mott-Schottky method. Example Mott Schottky plots (c) and approximate defect carrier density (d) of cuprous oxides. Error bars are the standard error of three replicate experiments.

charge) and increased in electronic resistance with increasing Al content in the alloy (Figure 9b).

Soluble corrosion products – ICP-OES.—Soluble release of Cu and Al at selected time-points following open circuit full-immersion exposure to artificial perspiration are shown in Figures 10a and 10b, respectively. Triplicate measurements using separate samples of soluble Cu release at 96, 130, and 144 h are shown in Figure 11. Soluble copper release (Figure 10a) from Cu-Al was nearly linear with time for ≥ 2 at% Al Cu-Al alloys. However, Cu release rates (slope) diminished after 96 h for Cu-0.2Al and Cu. Al was not detected as a soluble species from Cu-Al above the limit of detection (0.2 ppm) consistent

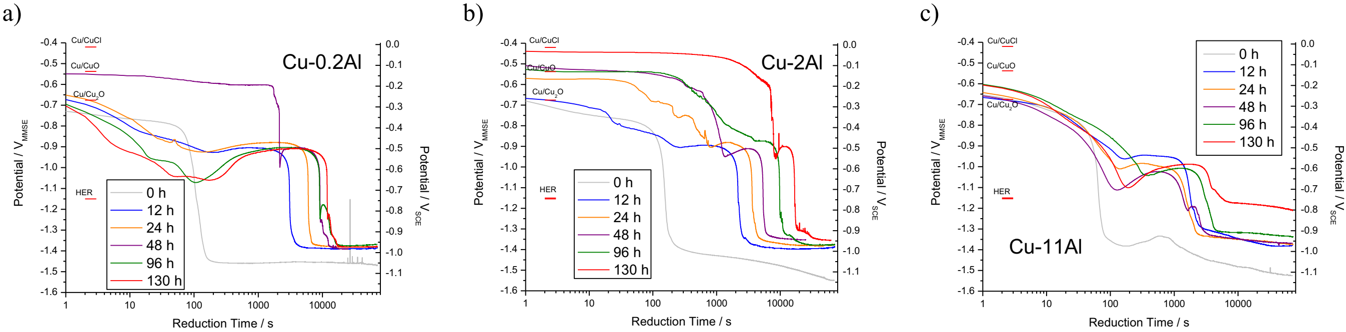

Figure 8. Coulometric reduction curves of Cu-Al alloys following open circuit exposure to artificial perspiration at specified durations up to 130 h. a) Cu-0.2Al, b) Cu-2Al, c) Cu-11Al. Reduction media was a deaerated boric/borate buffer at pH 8.4 with an applied cathodic current of 25 μA/cm^2. $Al_2O_3 \rightarrow Al$ $E_r = -2.6$ V_{MMSE}.

Downloaded on 2018-10-27 to IP 165.124.166.111 address. Redistribution subject to ECS terms of use (see ecsdl.org/site/terms_use) unless CC License in place (see abstract).

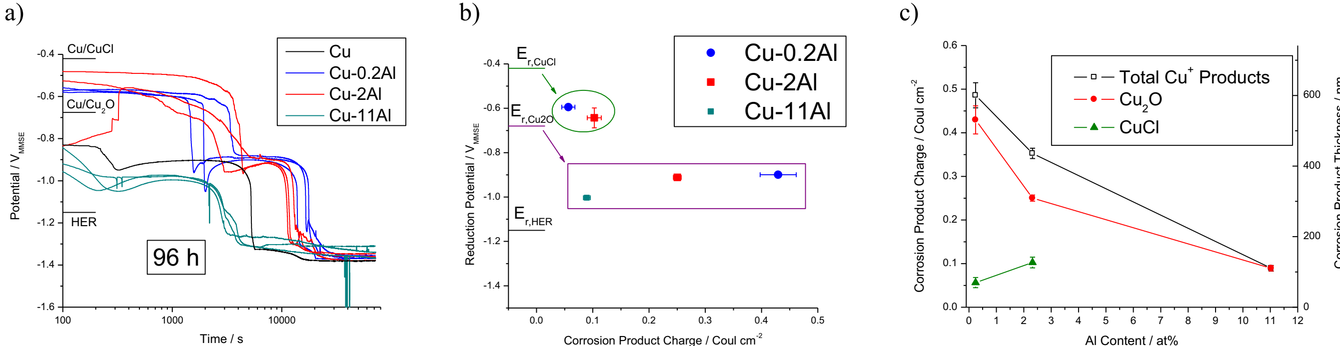

Figure 9. Coulometric reduction statistics at 96h in artificial perspiration. a) chronopotential curve, b) Reduction potentials and individual amounts of corrosion products expressed as charge density, and c) Total reducible corrosion product charge as a function of Al content and estimated thickness from Equation 4.

with prior work,[9,29,37] but was released in significant amounts from a pure Al sample (0.84 ± 0.06 ppm, Figure 11) subjected to the same exposure conditions.

Total anodic charge – corrosion rates in artificial perspiration.—Gravimetric mass loss measurements and impedance measurements of Cu-Al alloys following exposure to artificial perspiration are presented as anodic charge and inverse polarization resistance as a function of alloying content at 96 h in Figure 12a. Mass loss (mg/cm^2) over time is compared with a corresponding integrated anodic charge from EIS in Figure 12b. Cu-2Al had the greatest mass loss of all elements (Cu and Al) and alloys (Cu-Al). A cuprous (n = 1) assumption provided the best match between mass loss and derived anodic charge obtained independently from EIS measurements and corroborated by prior work.[30,38,44,45] Electrochemical impedance measurements on Cu-Al samples exposed to artificial perspiration also revealed Cu-2Al had the greatest corrosion rate ($1/R_p \propto i_{corr}$, Figure 12a). Cu and the other Cu-Al alloys had similar mass loss at 96 h.

Potentiodynamic polarization.—Potentiodynamic polarizations shown in Figure 13 illustrate that Al does not passivate Cu-Al alloys in artificial perspiration (pH 6.5) or HCl (pH 0). The potential window near the open circuit potential of Cu-Al alloys from −0.50 V_{SCE} to +0.25 V_{SCE} is shown in Figure 13. Al in the alloy does not appreciably

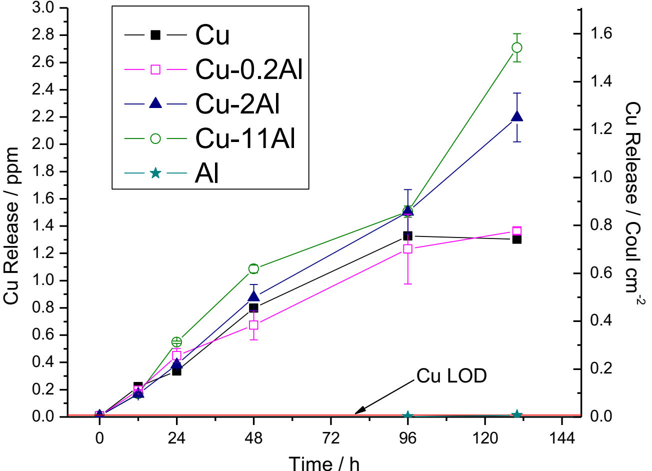

Figure 10. Soluble Cu release from Cu, Al, and Cu-Al alloys at set time points in artificial perspiration up to 130 h. Aliquots (15 mL) of separate samples taken at set time intervals and measured using ICP-OES. Error bars are standard error from three measurements per aliquot. Solid red line is the limit of detection for Cu: 17 ppb.

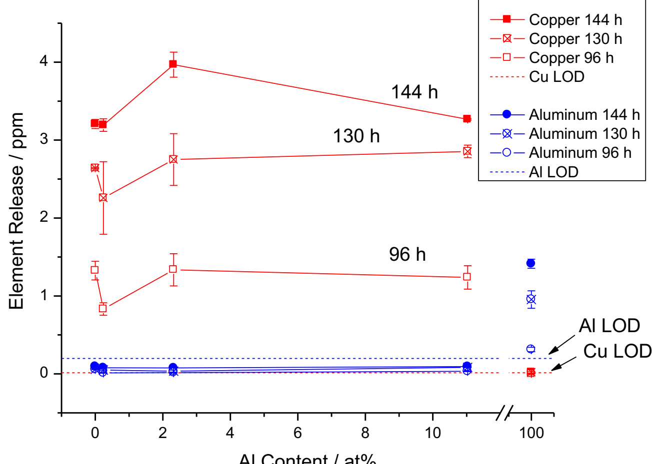

Figure 11. Soluble element release via ICP-OES as a function of Al content in the alloy. Error bars are the standard error of three replicate experiments. Cu and Al limits of detection are illustrated by red and blue dashed lines, respectively.

affect anodic kinetics. Notably however, Cu-Al alloys had increased cathodic reaction (ORR) rates on the bare metal surface in both artificial perspiration and hydrochloric acid compared to commercially pure Cu. Pure aluminum pits at its open circuit potential in both artificial perspiration and HCl and did not passivate in either solution revealing only ohmic controlled anodic dissolution. The surfaces of Al samples post-experiment were highly pitted with a significant amount (grams) of visible material loss. The native oxide on Al did not protect the surface in either artificial perspiration or 1 M HCl.

Galvanostatic anodic holds of Cu-Al alloys in artificial perspiration are given in Figure 14. Anodic dissolution was rendered more facile by the addition of Al to Cu-Al indicated by the reduced anodic potential for the same imposed anodic current density. The increased corrosion rates and cation Cu release of Cu-2Al may be ascribed to easier anodic dissolution due to Al alloying as shown by Figure 14.

Discussion

Aluminum as a solute in FCC solid solution with copper oxidizes and is located in one of three probable states: (1) Al may oxidize to form its own oxide (Al_2O_3) in a physical mixture or stratified layers with copper oxidation products (Cu_2O), (2) Al and Cu may combine to form a mixed oxide or spinel phase (e.g., $CuAlO_2$, or $CuAl_2O_4$) which are more thermodynamically stable than the individual oxides (Table I) but may be kinetically limited at room temperatures and short

Downloaded on 2018-10-27 to IP 165.124.166.111 address. Redistribution subject to ECS terms of use (see ecsdl.org/site/terms_use) unless CC License in place (see abstract).

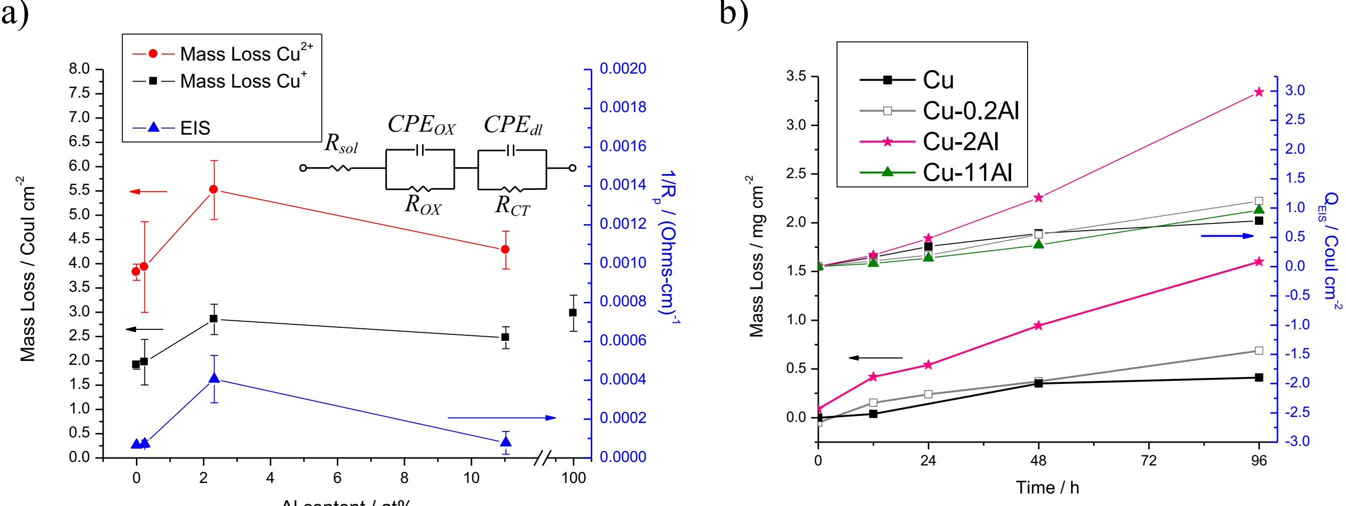

Figure 12. Total anodic charge measurements of Cu-Al alloys exposed at open circuit to artificial perspiration a) after 96 h of gravimetric mass loss compared to inverse polarization resistance determined with EIS and b) over time up to 96 h. Inverse polarization resistance (a) and integrated anodic charge (b) were calculated from equivalent circuit fits (circuit shown in inset of a). Error bars are standard error of triplicate measurements. Stern-Geary coefficient, B, assumed as 25 mV. Equivalent circuit elements R_s = solution resistance, CPE_{ox} = oxide constant phase element, R_{ox} = oxide resistance, CPE_{dl} = double layer constant phase element. R_{ct} = charge transfer resistance. $R_p = R_{ox} + R_{ct}$.

duration (days), or (3), Al may become captured within the primary Cu (or solvent) oxide phase. Al_2O_3 does not have any thermodynamic solubility in Cu_2O.[46] These individual fates would have consequences on both the compositional and structural nature of the corrosion products formed on the alloy phase, and hence, may strongly influence corrosion and cation release properties of the alloy. By interrogating several alloy compositions, not only can we determine the fate of the solute element, Al, but also its role on corrosion of aluminum copper alloys.

From the evidence presented here based upon GIXRD, CR, XPS, and MS, Al becomes a substitutional cation defect in the cuprite layer. Solute-enrichment is the fate of Al because there is evidence of quantifiable physical, chemical, and electrochemical modifications to cuprite. GIXRD did not show peaks which would correspond to $CuAlO_2$ (PDF 00-035-1401) or $CuAl_2O_4$ (PDF 00-033-0448) and no individual phase of oxidized Al (e.g., Al_2O_3) was observed, which is consistent with other findings in the literature at even longer exposure times (880 h,).[47] Pure Al does not form a stable passive layer and pits at open circuit in artificial perspiration (Figure 13a), suggesting that the protective mechanism (Figure 9c) is not from an stoichiometric oxide layer consisting pure Al such as Al_2O_3. In addition, CuCl and modified cuprite were the only corrosion product phases observed despite using multiple methodologies including crystal diffraction (Figure 4), Raman spectroscopy (Figure 3), electrochemical (Figure 8) and XPS characterization (Figure 6).

Kinetic conditions required for solute-capture of Al in Cu_2O.— The conditions for solute capture may be conceptualized by considering the conditions required to reach chemical equilibrium (or quasi-equilibrium given by metastable states). Figure 15 visually illustrates the conditions required for solute capture for a growing cuprous oxide in an electrochemical system. Within this theoretical framework, if the velocity of the growing oxide/metal or oxide/fluid interface, which can be related to some fraction of the corrosion current (i_{corr}) that contributes to scale growth is faster than the ability of the solute to diffuse to a neighboring solute to form a separate pure phase separated oxide phase then it can be expected to be solute trapped. The speed of foreign cation rearrangement can be assessed by considering a diffusion

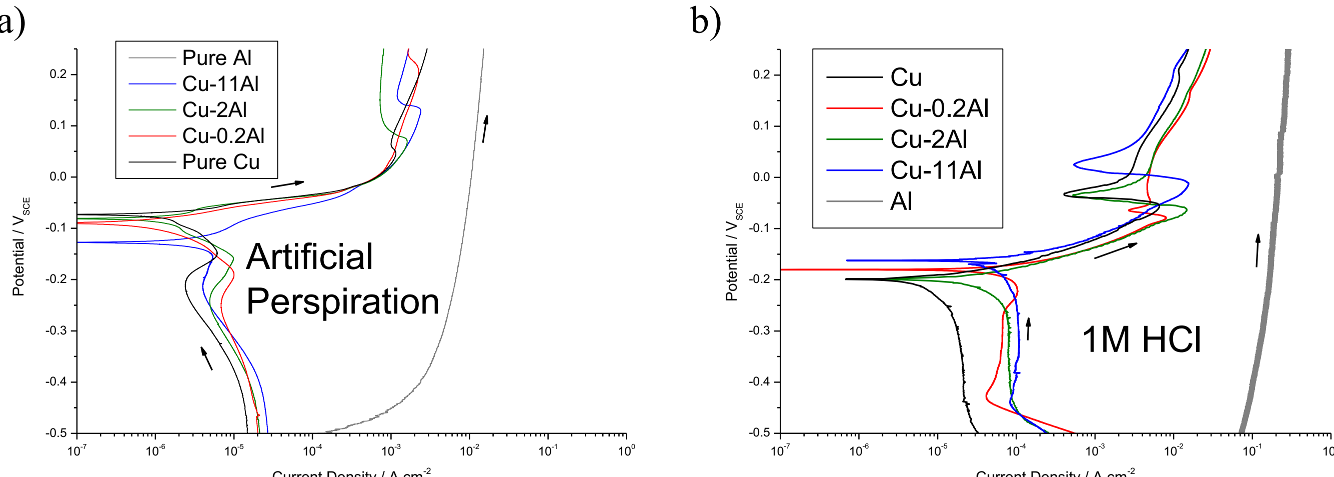

Figure 13. Potentiodynamic polarization scans of Cu-Al alloys in a) artificial perspiration, and b) 1M HCl. Scan rate 0.1667 mV/s. Samples were held at $-1.5\ V_{SCE}$ for 10 min prior to upward scan.

Downloaded on 2018-10-27 to IP 165.124.166.111 address. Redistribution subject to ECS terms of use (see ecsdl.org/site/terms_use) unless CC License in place (see abstract).

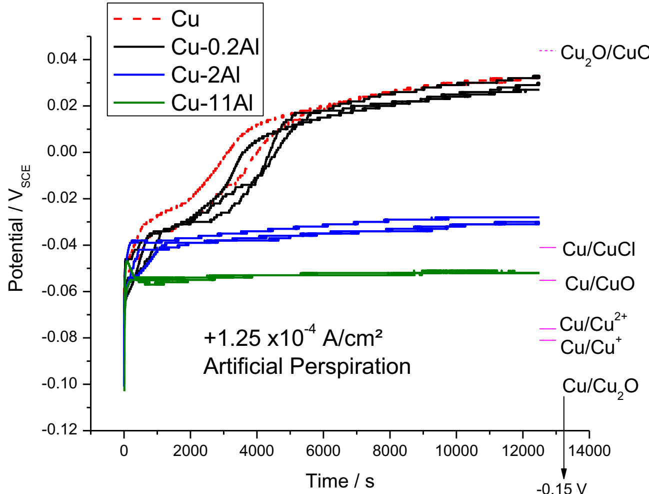

Figure 14. Galvanostatic anodic holds of Cu-Al alloys in naturally-aerated artificial perspiration. The anodic current applied was 1.25×10^{-4} mA/cm^2.

coefficient (D) and a required jump distance (a) as D/a. If the growth velocity then exceeds D/a then the solute becomes captured by the growing interface.[48] The exact jump distance is uncertain. In Figure 15, several jump distances are considered in our calculations. In the range of these experiments the oxide growth current densities derived from CR results (highlighted in Figure 8) are on the order of 10^{-6} to 10^{-7} A/cm^2. A reasonable assumption for the diffusion rate of Al in the solid state cuprous oxide is in the range of 10^{-20} to 10^{-30} cm^2/s which are similar to the diffusion rates for oxide systems such as Cr in NiO (also p-type).[27,49] For a Cu-Al system, the theoretical requirements for solute capture are indeed met (Figure 15) under typical film growth conditions. It is therefore possible that Al^{3+} becomes an isolated cation defect in the growing Cu_2O layer during open circuit corrosion in artificial perspiration. Directly, changes in Cu_2O lattice parameter suggest this. Indirectly, more negative reduction potentials during CR suggest more thermodynamically stable $(Cu,Al)_2O$ rather than Cu_2O.

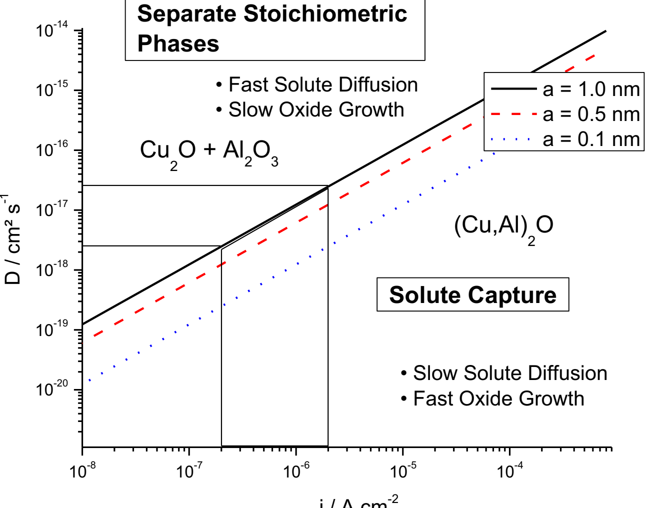

Figure 15. Theoretical requirements for solute capture of an element in a growing oxide for various jump distances (a). The diffusion coefficient (D) of the solute in the growing oxide is compared with the current density attributed to the growing oxide interface (i). Should the advancement of the oxide front exceed the speed at which the solute can diffuse to form its own oxide, the solute becomes captured as a substitutional defect in the oxide.[27]

Concerning the other potential fates, a physical mixture of phase pure Al_2O_3 and Cu_2O would require greater free energy change due to the additional interfaces (excess interfacial energy of an interface). While alumina (Al_2O_3) and $CuAlO_2$ and $CuAl_2O_4$ may be more thermodynamically favorable (Table I), these phases were not detected with Raman spectroscopy (Figure 3), GIXRD (PDF 00-035-1401 and 00-033-0448, Figure 4), or suggested from electrochemical measurements (Figure 7, Figure 8). The kinetic barriers or stoichiometric constraints (Cu, Al, O chemical fractions available) during dissolution may not be favorable to form these compounds either directly via solid state or indirectly via chemical precipitation from aqueous phase on the actively corroding Cu-Al surface. Solute capture (i.e. doping) of Al cations in cuprite is likely and would have consequences on the electrical and structural properties of the oxide layer formed on Cu-Al alloy, which would then affect the tarnish and corrosion behavior of the alloy.

The fate of Al following corrosion in artificial perspiration: solute capture.—The evidence of physical, chemical, and electronic modifications of the cuprite layer all suggest that an aluminum-enriched or doped Cu_2O is formed via solute capture following open circuit corrosion of Cu-Al in artificial perspiration.

Physical modifications of Cu_2O.—Cuprite lattice shrinkage.—Cuprous oxide is a cubic structure with Cu cations located on an FCC sublattice and oxygen anions on a BCC sublattice translated one-quarter body diagonal. The most compact lattice plane is (111) also having the greatest diffraction multiplicity. GIXRD revealed that the 2Θ peak position relating to the lattice reflection of the (111) plane of cuprite was shifted to higher values (Figure 4). A Bragg's law calculation reveals a slightly more compact lattice structure with Al indicated by a shorter distance ($\Delta d = 0.01$ Angstroms) between (111) lattice planes of this cubic crystal. The full width at half max of the cuprite (111) peak is greater on Cu-11Al (see Figure 5), indicating that this lattice spacing is more distributed by the presence of Al possibly due to lattice distortions. The lattice is less uniform with possibly bounded lattice strain at the oxide/metal interface indicated by the broader peak with more Al in the cuprite lattice. These results concerning the structure of the cuprous oxide are suggestive of cation substitution of Al in place of some Cu atoms. The degree of enrichment of Al in the cuprite layer can be investigated with quantitative chemical analysis of photoelectron measurements.

Al-Enrichment.—X-ray generated PE spectra (Table IV, Figure 6) were quantified to determine the relative cation fractions of Cu and Al in the films formed in artificial perspiration. The cation fraction of Al in the oxide on Cu-Al alloys tested in this study were compared with the Al content (at%) in the alloy (Figure 16). This figure shows the average cation fraction of Al in the film through its thickness from several sputter depths (Table IV). The position of the metal phase was determined from the Cu_{LMM} Auger excitation (when KE = 918.6 eV). The results were fit to a model presented by Kirchheim et al.[50] to quantify the enrichment of Cr in Fe-oxide films undergoing steady-state dissolution. Equation 7 describes the degree of enrichment of Al in the surface film for a Cu-Al alloy.

$$x_{Al,f} = \frac{\beta x_{Al,a}}{1 - x_{Al,a} + \beta x_{Al,a}} \quad [7]$$

Where β is the ratio of the ion-specific dissolution rates (i_{Cu}/i_{Al}) under steady-state conditions. The chemical dissolution rate of Al^{3+} from Cu_2O is unknown and would imply Al^{3+} depletion not enrichment. However, the driving force for Al^{3+} formation is high. Moreover, if the rate-determining step is cation diffusion through a conformal film, under the assumptions of the Cabrera-Mott model,[51] β may be described by the relative cation diffusivities through the film (D_{Cu}/D_{Al}).[50] The subscripts f and a denote assignment to the element in the corrosion product film or alloy, respectively. The enrichment factor β was fit using Equation 7 from the sum of least squares regression using XPS cation fractions and alloy data values. The fit value of β obtained was 1.9, meaning that Cu was roughly twice as likely to be dissolved in the electrolyte compared to Al. Chemical stability diagrams show

Downloaded on 2018-10-27 to IP 165.124.166.111 address. Redistribution subject to ECS terms of use (see ecsdl.org/site/terms_use) unless CC License in place (see abstract).

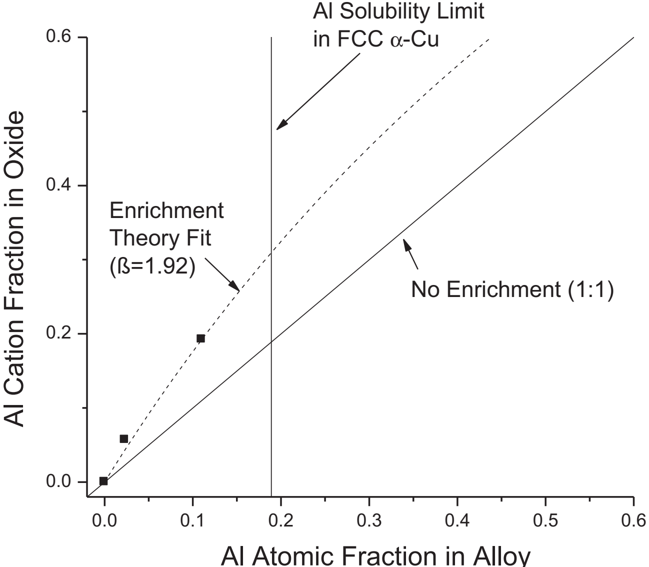

Figure 16. Solute enrichment of Al in cuprous oxide. Aluminum cation fractions determined via XPS (Table IV) of Al in the cuprite (Cu_2O) layer. Solute enrichment factor was fit using Equation 7.[50,54]

(Figure 17) that in near neutral pH solutions that Cu_2O will precipitate first during anodic dissolution, followed by the possibility of hydrated Al_2O_3 compounds. It is therefore unlikely in minor amounts of Al (≤12 at%) that Al_2O_3 will be able to form if a metastable phase of Al-doped Cu_2O is a possible alternative.

Electronic modifications of Cu_2O with Al^{3+} solute capture.—Increase in reduction overpotential.—Not only does the thickness of the cuprite layer decrease with increasing Al content in the α-phase (Figure 9c), but the reduction potential also decreased (Figure 9b). An increase in electronic resistance of the oxide would manifest as an increased overvoltage, lowering the potential at which the oxide is galvanostatically reduced. Cathodic reduction indeed revealed that oxide films became more difficult to reduce with increasing Al content (Figure 9b). This result implies that the electronic defect structure of the semiconducting oxide, i.e. the charge carriers, are influenced by Al content.

Decrease in charge carrier density.—Cuprite (Cu_2O) is a metal-deficient p-type semiconducting oxide.[28] Positively-charge electron holes (p) carry electronic charge while negatively charged cation vacancies ($V_{Cu}^{'}$) are the dominant ionic defect.[28] The Mott-Schottky method can be used to estimate the density of electronic charge carriers in a semiconductor.[34] While the exact defect density cannot be accurately measured from electrochemically grown films on metal substrates,[36] relative changes in the defect nature of this semiconducting cuprous oxide were evaluated with a Mott-Schottky analysis (Figure 7). A decreased number of charge carriers, i.e. holes, were measured from Cu_2O films grown on the Cu-Al alloys. These results also support that Al^{3+} is likely present in the cuprous oxide cation sublattice either substitutionally in the place of Cu^+ cations or replacing Cu^+ cation vacancies which in turn affect the electronic structure of this cuprous oxide. The presence of substitutional Al cations in the oxide have consequences to the electronic structure as measured using the Mott-Schottky method. The defect chemistry of the cuprous oxide is modified by solute capture, i.e. doping, of Al^{3+} which has subsequent effects on corrosion products formed on the alloy.

Consequences of solute capture.—*Defect chemistry and aliovalent solute effects in cuprous oxide.*—The change in defect chemistry of cuprite due to Al substitution in the cuprous oxide cation sublattice is illustrated in Figure 18. The metal-deficient vacancy formation reaction is given by Equation 8. The equilibrium defect concentrations follow the thermodynamic relation in Equation 9 for a cuprous oxide with dominant cation vacancies.

$$\frac{1}{2}Cu_2O + V_{Cu}^{'} + h^+ = \frac{1}{4}O_2 \qquad [8]$$

$$[V_{Cu}^{'}][h^+] = \frac{pO_2^{1/4}}{K_{Cu_2O}} \qquad [9]$$

Where $[V^{'}_{Cu}]$ is the concentration of Cu^+ vacancies, $[h^+]$ is the hole concentration, pO_2 is the partial pressure of oxygen, and K_{Cu_2O} is the equilibrium constant of the reaction. Increasing the doping of trivalent Al as a substitutional cation in the Cu_2O lattice leads to an increase in Cu cation vacancies ($V^{'}_{Cu}$) to maintain charge neutrality (Figure 18). For a given volume of Cu_2O, the amount of total oxidized Cu as

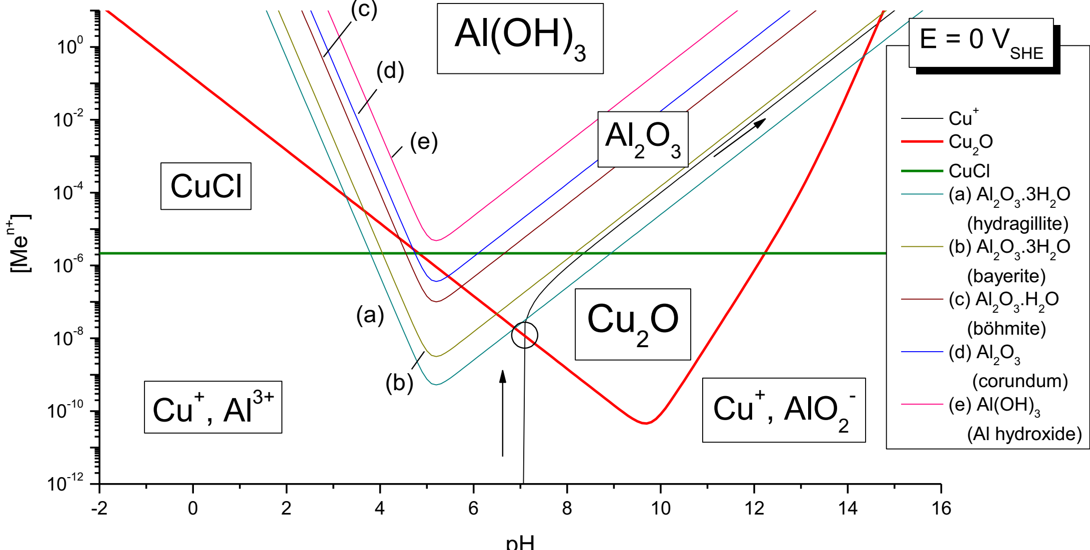

Figure 17. Superimposed chemical stability diagrams[55] of Cu and Al oxides as a function of pH with $[Cl^-] = 0.086$ M (artificial perspiration). Metal dissolution trajectory is indicated by arrows. Equilibrium products calculated for a potential of 0 V_{SHE}. The point of first chemical precipitation of an oxide is circled.

Downloaded on 2018-10-27 to IP 165.124.166.111 address. Redistribution subject to ECS terms of use (see ecsdl.org/site/terms_use) unless CC License in place (see abstract).

a)

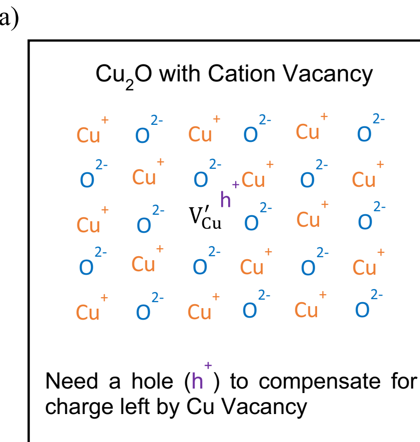

b)

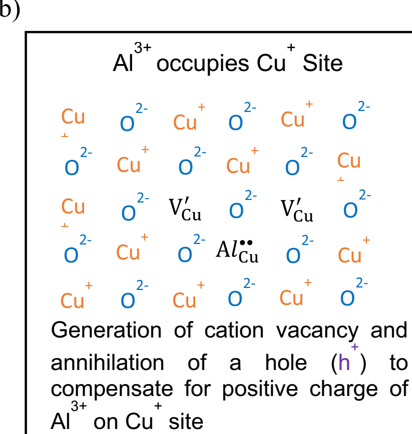

Figure 18. Schematic illustration of aluminum doping effects on cuprite electronic properties. Effect of intrinsic defects (a) compared with Al-doped (b) on the equilibrium defect chemistry.

soluble ions increases (Figure 10a) as these cation vacancies are created. Consequently, to maintain equilibrium via the law of mass action, and with a constant partial pressure (activity) of oxygen the number of holes (h^+, charge carrier) decreases according to Equation 9. Al doping results in an increase in cation vacancies and a decrease in charge carrier density thereby decreasing electronic conduction.[28,47] However, the mobility of these extra cation vacancies is reduced through electrostatic interactions with Al^{3+}. Density-functional calculations have shown that substitutional Al cations ($Al^{2+}{}_{Cu}$) strongly binds with two copper cation vacancies with a binding energy of 3.3 eV, thus greatly reducing vacancy mobility.[52] Inhibited electronic and ionic mobility reduces the kinetically-limited thickness of the Cu_2O corrosion product (Figure 9c). Mott-Schottky analysis corroborates this effect (Figure 7). The nature of the fate of the elements is indeed affected by Al; the thinner Al-modified cuprite films promote improved tarnish-resistance while simultaneous enabling soluble Cu release over additional oxide formation.

Tarnish resistance through thinning of cuprite layer.—Decreased thickness of cuprite layers with increasing Al content in α-Cu phase was also observed by Süry and Oswald.[47] They speculated that Al^{3+} cation substitutions in Cu_2O was responsible for the increased electronic resistance of the oxide[47] however until now, physical evidence to this claim has not been presented. The increased electronic resistance of the oxide is confirmed in the present work by CR and MS results given in Figures 9 and 7, respectively. Concerning the concept of generating a tarnish-resistant antimicrobial alloy by restricting growth of the oxide layer to undesirable levels, solid solution alloying of copper with oxide doping of aliovalent elements such as Al through solute capture is extremely promising in this regard.

Soluble copper and potential antimicrobial function.—While the increased resistance of the oxide film (Figure 9b) contributed to thinner Cu_2O which became more difficult to form, Cu ions continued to be released through this layer (Figure 11). An antimicrobial surface must maintain a sustained corrosion rate in order to be continuously functional. The thinner oxide and decreased thickness with increasing Al content coupled with a similar corrosion rate altered the corroding system to produce more soluble Cu ions relative to oxide formation. Greater Al contents would be expected to increase this effect but may be limited by solid-solution alloying limits. In this regard Cu with 11 at% Al effectively formed a 'leaky' stable oxide film through which soluble Cu is released, facilitating a tarnish-resistant and continually antimicrobial surface on the Cu-11Al alloy. Further study is required regarding chemistry and structure of air-formed thin films with abrasion and wear testing for these alloys which are critical for the future development of antimicrobial high-touch surfaces.

Conclusions

- The fate of Al following corrosion in artificial perspiration is solute-captured Al^{3+} cations in the cuprous oxide layer evidenced by (1) structural modifications determined with GIXRD, (2) electrochemical modifications to the oxide layer via coulometric reduction, (3) the presence of Al in the cuprous oxide layer identified through X-ray photoelectron spectroscopy, and (4) changes in the defect chemistry of the p-type cuprous oxide revealed by Mott-Schottky analysis.
- Al in the cuprite layer decreased the corrosion product thickness consistent with increased electronic and ionic resistivity due to dopant effects of substitutional Al cations on the Cu cation sublattice reducing the amount of electron holes and reducing cation vacancy ionic mobility through binding with metal vacancies. This results in thinner oxides while soluble Cu release remained approximately equal to pure Cu.
- Implantation of Al from the alloy into the cuprous oxide layer formed a more tarnish-resistant surface oxide which was thinner, had greater electronic resistance, and more difficult to electrochemically reduce with increasing Al content.
- Modifying the copper oxide layer with Al solute can alter the corrosion products formed on the surface of a Cu-Al alloy facilitating a tarnish-resistant layer without affecting soluble Cu release desirable for antimicrobial function.

Acknowledgments

This project was funded by the National Science Foundation (DMR-1309999) with Program Director Dr. Lynnette Madsen. Alloys were fabricated by the Materials Preparation Center at Ames Laboratory. Caelan Ryberg is gratefully acknowledged for laboratory assistance. Members of the Center for Electrochemical Science and Engineering (CESE) are thanked for various assistance and helpful discussions.

ORCID

M. J. Hutchison https://orcid.org/0000-0001-7057-4825
J. R. Scully https://orcid.org/0000-0001-5353-766X

References

1. H. T. Michels, W. Moran, and J. Michel, *Int. J. Met.*, 47 (2008).
2. H. T. Michels, S. A. Wilks, J. O. Noyce, and C. W. Keevil, in *Copper for the 21st Century*, p. 27, The Minerals, Metals & Materials Society, New Orleans, Louisiana (2005).
3. H. T. Michels, *ASTM Stand. News*, **34**, 28 (2006).
4. E. Sukkar, *Pharm. J.*, **13** (2013).

Downloaded on 2018-10-27 to IP 165.124.166.111 address. Redistribution subject to ECS terms of use (see ecsdl.org/site/terms_use) unless CC License in place (see abstract).

5. J. O'Neill, *Antimicrobial Resistance: Tackling a crisis for the health and wealth of nations*, HM Government, Wellcome Trust, (2014).
6. P. J. Kuhn, *Diagn. Med.*, **6**, 62 (1983).
7. S. S. Magill et al., *N. Engl. J. Med.*, **370**, 1198 (2014).
8. H. T. Michels and C. A. Michels, *Microbiology*, **10** (2016).
9. L. L. Foster and J. R. Scully, *Corrosion*, **72**, 1095 (2016).
10. R. F. North and M. J. Pryor, *Corros. Sci.*, **10**, 297 (1970).
11. W. A. Badawy, M. M. El-Rabiei, and H. Nady, *Electrochimica Acta*, **120**, 39 (2014).
12. W. A. Badawy, R. M. El-Sherif, and H. Shehata, *Electrochimica Acta*, **54**, 4501 (2009).
13. V. M. Villapún, L. G. Dover, A. Cross, and S. González, *Materials*, **9**, 736 (2016).
14. W. A. Badawy, R. M. El-Sherif, and H. Shehata, *J. Appl. Electrochem.*, **37**, 1099 (2007).
15. O. F. M. Benatti, W. G. Miranda Jr, and A. Muench, *J. Prosthet. Dent.*, **84**, 360 (2000).
16. Copper Development Association, *Copper and its Alloys Engineering and Technology*, 2nd ed., (1949).
17. Copper Development Association, *Wrought and Cast Copper Alloys*, https://alloys.copper.org/.
18. *Copper Data*, Copper Development Association, (1949).
19. A. M. Alfantazi, T. M. Ahmed, and D. Tromans, *Mater. Des.*, **30**, 2425 (2009).
20. M. Schumacher, (1979) http://books.google.com/books?id=HNRRAAAAMAAJ.
21. G. S. Duffó and S. B. Farina, *Mater. Chem. Phys.*, **115**, 235 (2009).
22. C. Young-Gab, P. Su-Il, and K. Chang-Ha, *Mater. Lett.*, **20**, 265 (1994).
23. T. Chang, G. Herting, Y. Jin, C. Leygraf, and I. Odnevall Wallinder, *Corros. Sci.*, (2018) http://linkinghub.elsevier.com/retrieve/pii/S0010938X17321005.
24. T. Chang, I. O. Wallinder, Y. Jin, and C. Leygraf, *Corros. Sci.*, **131**, 94 (2018).
25. M. D. Sanderson and J. C. Scully, *Oxid. Met.*, **3**, 59 (1971).
26. A. G. Tyurin, *Prot. Met.*, **44**, 292 (2008).
27. T. K. Andersen et al., *ACS Appl. Mater. Interfaces*, **10**, 5949 (2018).
28. E. McCafferty, *Introduction to Corrosion Science*, Springer New York, (2010) https://books.google.com/books?id=g9oXcE-gQKUC.
29. L. L. Foster, M. Hutchison, and J. R. Scully, *Corrosion*, **72**, 51 (2016).
30. M. J. Hutchison, P. Zhou, K. Ogle, and J. R. Scully, *Electrochimica Acta*, (2017) http://www.sciencedirect.com/science/article/pii/S0013468617308496.
31. D. J. Horton and J. R. Scully, *Metall. Mater. Trans. -Phys. Metall. Mater. Sci.*, **43A**, 2706 (2012).
32. British Standards Institute, *BS EN 1811: Reference test method for release of nickel from all post assemblies which are inserted into pierced parts of the human body and articles intended to come into direct and prolonged contact with the skin*, (2008).
33. J. F. Moulder and J. Chastain, *Handbook of X-ray Photoelectron Spectroscopy: A Reference Book of Standard Spectra for Identification and Interpretation of XPS Data*, Physical Electronics Division, Perkin-Elmer Corporation, (1992) https://books.google.com/books?id=A_XGQgAACAAJ.
34. K. Gelderman, L. Lee, and S. W. Donne, *J. Chem. Educ.*, **84**, 685 (2007).
35. S. Laidoudi et al., *Semicond. Sci. Technol.*, **28**, 115005 (2013).
36. W. Schmickler, *Interfacial Electrochemistry*, Oxford University Press, USA, (1996) https://books.google.com/books?id=iJh1mAEACAAJ.
37. D. J. Horton, H. Ha, L. L. Foster, H. J. Bindig, and J. R. Scully, *Electrochimica Acta*, **169**, 351 (2015).
38. P. Zhou, M. J. Hutchison, J. R. Scully, and K. Ogle, *Electrochimica Acta*, **191**, 548 (2016).
39. L. G. Sillén, A. E. Martell, and J. Bjerrum, *Stability constants of metal-ion complexes*, Chemical Society, London, (1964).
40. *ASTM G1-03(2011) Standard Practice for Preparing, Cleaning, and Evaluating Corrosion Test Specimens*, ASTM International, (2011).
41. *Database of Raman Spectroscopy, X-ray Diffraction and Chemistry of Minerals*, RRUFF Project http://rruff.info/.
42. F. Ospitali et al., *J. Raman Spectrosc.*, **43**, 1596 (2012).
43. G. S. Rohrer, *Structure and Bonding in Crystalline Materials*, Cambridge University Press, (2001) https://books.google.com/books?id=a0jPqKw2Zx8C.
44. P. Zhou, M. J. Hutchison, J. W. Erning, J. R. Scully, and K. Ogle, *Electrochimica Acta*, **229**, 141 (2017).
45. O. Gharbi, N. Birbilis, and K. Ogle, *J. Electrochem. Soc.*, **163**, C240 (2016).
46. C. W. Bale et al., *Calphad*, **54**, 35 (2016).
47. P. Süry and H. R. Oswald, *Corros. Sci.*, **12**, 77 (1972).
48. J. C. Baker and J. W. Cahn, *Acta Metall.*, **17**, 575 (1969).
49. S. Mrowec, *Defects and diffusion in solids: an introduction*, Elsevier Scientific Pub. Co., (1980) https://books.google.com/books?id=UQtRAAAAMAAJ.
50. R. Kirchheim et al., *Corros. Sci.*, **29**, 899 (1989).
51. N. Cabrera and N. F. Mott, *Rep. Prog. Phys.*, **12**, 163 (1949).
52. A. F. Wright and J. S. Nelson, *J. Appl. Phys.*, **92**, 5849 (2002).
53. R. L. Frost, *Spectrochim. Acta. A. Mol. Biomol. Spectrosc.*, **59**, 1195 (2003).
54. M. Seo and N. Sato, *Langmuir*, **3**, 917 (1987).
55. P. Marcel, *Atlas of Electrochemical Equilibria in Aqueous Solutions*, Second English Edition., p. 644, National Association of Corrosion Engineers, Houston, TX, (1974).

Downloaded on 2018-10-27 to IP 165.124.166.111 address. Redistribution subject to ECS terms of use (see ecsdl.org/site/terms_use) unless CC License in place (see abstract).